

# Fast and Continuous Detection of Single Microwave Photons via Photo-assisted Quasiparticle Tunneling to a Superconducting Island

J. Basset,\* O. Stanisavljević, J. Gabelli, M. Aprili, and J. Estève  
*Université Paris-Saclay, CNRS, Laboratoire de Physique des Solides, 91405 Orsay, France*  
(Dated: November 24, 2025)

We demonstrate a single-photon detector operating in the microwave domain, based on photo-assisted quasiparticle tunneling events that poison a superconducting island. The detection relies on continuously monitoring the island’s charge parity using microwave reflectometry. This scheme achieves 10% detection efficiency with sub 50 ns time resolution and short dead time ( $\sim 1 \mu\text{s}$ ), for microwave photons at 10 GHz. The detector features three junctions connected to a superconducting island, which together carry out photoelectric conversion and charge readout. The enhanced light–matter coupling, crucial to photon to quasiparticle conversion, is provided by a granular aluminum–based high-impedance microwave resonator. The time resolved detection of itinerant microwave photon opens up new perspectives in quantum sensing, microwave quantum optics, readout of superconducting qubits and mesoscopic physics.

The ability to detect single microwave photons is essential for advancing quantum optics, quantum information processing, and quantum thermodynamics in superconducting circuits [1]. In contrast to the optical domain, where high-efficiency single-photon detectors are mature and widely deployed [2], microwave single-photon detection remains a central challenge due to the extremely low photon energy and the difficulty of isolating individual quantum events from thermal and measurement-induced noise at cryogenic temperatures. Robust fast and efficient microwave photon detection would not only enhance the capabilities of circuit quantum electrodynamics (cQED) platforms and microwave quantum optics [3] but also open new perspectives in quantum sensing [4] and mesoscopic physics [5].

Several detection strategies have been developed to tackle this challenge. Architectures based on superconducting qubits have demonstrated high sensitivity and photon number resolution, using projective qubit measurements to register single-photon absorption events [6–12]. Alternative approaches have been considered including Josephson photomultipliers [13], current-biased detectors [14–16], bifurcation amplifier [17], semiconducting quantum dots [18, 19] and calorimetric schemes [20, 21], each offering a distinct compromise between speed, fidelity, and experimental complexity.

In this work, we experimentally demonstrate a detection mechanism based on photoassisted quasiparticle tunneling in a superconducting island, which enables continuous and fast detection of single microwave photons. In the detector’s ready state, the island carries an even charge. The absorption of an incident photon through a photo-assisted tunneling of a single quasiparticle switches the island’s charge parity from even to odd, as previously demonstrated for the detection of much higher energy photon in the infrared domain [22, 23]. This parity transition is continuously monitored via the reflection of a microwave readout signal, following the principle of a radio-frequency single-electron transistor (RF-SET) [24, 25] or

single Cooper pair transistor (SCPT) [26–30]. In this way, the detector produces a real-time signal in which photon absorption manifests as a distinct pulse, directly analogous to the “click” of an optical single-photon detector.

Central to the detector’s performance is a high-impedance granular aluminum (grAl) resonator [31], which transforms the  $50 \Omega$  input impedance to match that of the tunnel junction responsible for photon-to-charge conversion [32]. A second grAl resonator is used for charge readout, enabling rapid detection of the island’s charge parity and providing a photon-arrival time resolution of 50 ns. In addition to fast and efficient microwave photon detection, this architecture allows detailed investigation of electron–photon interactions in superconducting nanostructures. The ability to resolve individual photo-assisted tunneling events enables detailed studies of electron transport in high-impedance environments where light couples strongly to electronic degrees of freedom, potentially revealing phenomena such as the Franck–Condon blockade [33, 34]. Moreover, photon-driven charge transfer in this system could enable on-demand quantized current sources, with potential applications in metrology [35].

**Principle of the experiment**— The operating principle of the detector is illustrated in Fig. 1. Details about the device fabrication can be found in the Supplementary Material. A superconducting island is connected through three junctions to the detector input port, the readout port, and ground (Fig. 1a). During normal operation of the detector, the readout bias  $V_r$  is set to zero, and the gate voltage  $V_g$  is adjusted to maximize the critical current through the two junctions (JR, JD) forming the SCPT, thereby pinning the island potential to ground. The third junction (JC), referred to as the converter, is biased at  $V_c$  just below the onset of quasiparticle tunneling near the superconducting gap. In the ready state, the island carries even charge parity. An incoming photon at the detector input can be absorbed through a photo-

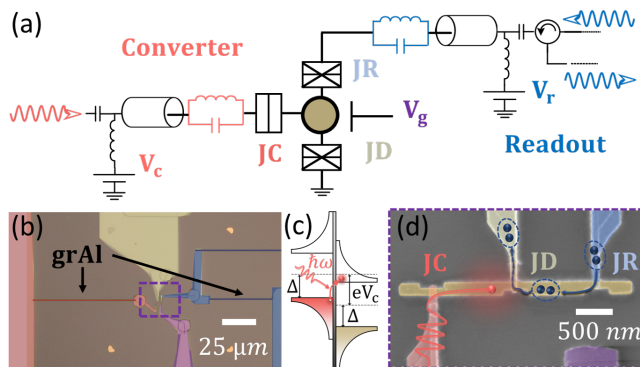


FIG. 1. **Detection principle and device.** (a) Simplified circuit diagram of the detector. An incoming microwave photon at the detector input is absorbed via photo-assisted tunneling into a superconducting island, inducing a quasiparticle-poisoning event. The resulting change in charge parity is continuously monitored through microwave reflectometry at the readout port. Three dc bias voltages ( $V_r$ ,  $V_c$ ,  $V_g$ ) tune the working point of the detector. (b) Optical micrograph of the device. Both converter and readout resonators are made of 700 nm wide, 20 nm thick granular aluminum wires with large kinetic inductance (0.5 nH/□). The converter resonator is 73  $\mu\text{m}$  long and the readout resonator is made of two sections, which are 48  $\mu\text{m}$  and 172  $\mu\text{m}$  long. (c) Energy diagram representation of the microwave photo-assisted tunneling process. (d) Scanning electron micrograph of the superconducting island and the three junctions JC, JR and JD. The gate appears in purple.

assisted tunneling (PAT) event at JC, generating a quasiparticle on the island (Fig. 1c) [36, 37]. The resulting charge parity flip modifies the impedance of the readout circuit until the quasiparticle leaves the island, after which the detector self-resets on a timescale of  $\sim 1 \mu\text{s}$ . Monitoring the reflection of a microwave tone from the readout circuit yields a square-pulse signal marking each photon-detection event.

The quarter-wavelength grAl resonator preceding JC provides impedance matching at  $\nu \approx 10 \text{ GHz}$  from the detector input to the junction. The photon to quasiparticle conversion efficiency reaches unity when the resonator coupling rate  $\kappa_c$  matches the PAT absorption rate through JC. We previously demonstrated an efficiency exceeding 80% [32] in a single junction device, and a comparable result was recently obtained with a double quantum dot [19]. For a junction coupled to a single mode resonator, the PAT rate scales with the junction conductance and the Franck-Condon factor  $\lambda^2 \exp(-\lambda^2)$ , where the dimensionless light-matter coupling constant  $\lambda = \sqrt{\pi Z_c / R_K}$  depends on the ratio between the mode's characteristic impedance  $Z_c$  and the quantum of resistance  $R_K = h/e^2$ . The Franck-Condon factor for elastic tunneling is simply  $\exp(-\lambda^2)$ . Large  $\lambda$  therefore enhances the PAT-to-elastic rate ratio and suppresses associated dark counts; our grAl resonator achieves  $\lambda = 0.63$ . The

converter junction, realized via triple oxidation, has a normal-state resistance of 6.4 M $\Omega$ . The other modes in the circuit, including the higher order modes of the converter resonator and the modes of the Cooper pair transistor, also induce a dynamical Coulomb blockade and reduce the PAT rate. Including all these effects, as detailed in the Supplementary Material, we evaluate a PAT rate of  $\kappa_j \approx 2\pi \times 10 \text{ MHz}$ , below the coupling rate, which we estimate to  $\kappa_c \approx 2\pi \times 70 \text{ MHz}$ . This rate mismatch limits the quantum efficiency around 50%, suggesting that further engineering could improve performance.

The quasiparticle generated by the PAT process flips the island's charge parity from even to odd. This parity switching suppresses the critical current of the SCPT, changing its microwave impedance, thus shifting the resonant frequency of the readout resonator. The resonator, also made of grAl, is designed to have a smaller light-matter coupling strength around 0.2 and a resonant frequency near 5.2 GHz. The two SCPT junctions, JR and JD, have normal-state resistances summing up to 136 k $\Omega$ . The island, fabricated from a thin (15 nm) aluminum layer, has an enhanced gap to suppress quasiparticle poisoning through JR and JD, which connect to thicker Al leads [38].

The reflection coefficient  $S_{11}$  upon the readout port is monitored with a probe tone nearly resonant with the readout resonator. Two types of measurements were conducted: one employing a Josephson Parametric Amplifier (JPA) on the returning path of the readout signal, and one without (see Supplementary Material for the detailed microwave setup). The probe amplitude is adjusted to obtain two well-separated signals in the IQ plane corresponding to each charge parity in less than 100 ns integration time. This behavior contrasts with standard RF-SET operation, which detects small charge offsets producing only minor  $S_{11}$  variations [24, 25]. Without JPA, we achieve a sensitivity of  $6 \times 10^{-6} e/\sqrt{\text{Hz}}$ , comparable to state-of-the-art RF-SETs [39].

Instead, the readout is similar to previous real time parity detection in SCPTs [29, 30] and in charge sensitive transmon qubits [40, 41]. In our case, the charge detector operates in the Cooper pair box regime, chosen to maximize readout speed. The detector self-resets to the even-parity state within 1  $\mu\text{s}$  as previously observed [29]. Charge-parity readout can be performed continuously or in pulsed mode, in which case a readout pulse follows the signal pulse at the detector input. Optimization of the detector performance primarily involves tuning the readout power and integration time to balance detection efficiency and dark counts.

**Experimental Results**— Figure 2a shows one quadrature of the reflected readout signal as a function of gate and dc bias across the SCPT. Coulomb diamonds are observed, periodic in gate voltage with a period corresponding to a  $2e$  change in island charge. In the presence of an additional quasiparticle of charge  $e$ , the en-

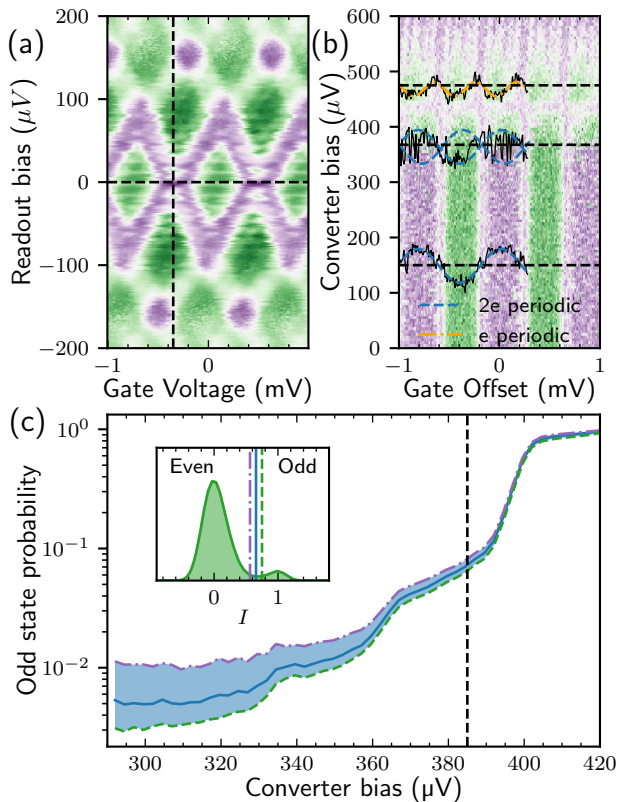


FIG. 2. **Charge stability with voltages.** (a) Dependence of one quadrature,  $I$ , of the reflected readout signal on gate voltage and readout bias at zero converter bias. The observed Coulomb diamonds are  $2e$  periodic and delimit stable charge states with a well defined number of Cooper pairs. The crosshair indicates the detector operating bias point. (b) Dependence of the readout signal at zero readout bias on gate voltage and converter bias. Selected gate voltage line cuts are overlaid with  $2e$  (blue) and  $e$ -periodic (yellow) sinusoidal curves, illustrating the transition from a  $2e$  to  $e$  periodic response. (c) Probability of the odd charge state as a function of converter bias  $V_c$  in absence of photon irradiation. The inset shows the histogram of the readout signal at  $V_c = 385 \mu\text{V}$  integrated for 100 ns using the JPA setup. The measured quadrature is rescaled and offset such that the two maxima are located at 0 and 1. The three vertical lines indicate the thresholds used to extract the odd-state probability  $p_1$  shown in the main plot. Each curve corresponds to the threshold lines indicated in the inset.

tire pattern shifts by half a period. From the diamond height, the charging energy of the SCPT is estimated to  $E_C \approx 20 \mu\text{eV}$ . The charge parity readout is operated at  $V_r = 0$ , while  $V_g$  is adjusted to maximize the SCPT critical current (see Fig. 2a). To maintain operation at this optimal point during the detector operation, the gate voltage is periodically adjusted every few seconds to compensate for slow charge-offset drift and for abrupt charge jumps of  $e$  occurring on minute timescales. The gate dependence of the reflection coefficient  $S_{11}$  is recorded and

compared to a reference waveform to extract the offset. When a voltage is applied to JC, an additional correction is applied based on the known capacitive lever arm, calibrated in a separate measurement.

We first examine the rate at which quasiparticles enter the island in the absence of any incident signal on the detector. Figure 2b shows the evolution of one quadrature of the reflected signal  $S_{11}$  as a function of the gate offset from the optimal point and the voltage  $V_c$  across the converter junction JC. As  $V_c$  approaches the superconducting gap, a transition from  $2e$ - to  $e$ -periodic gate modulation is observed, indicating the onset of quasiparticle poisoning. Each data point corresponds to a  $1 \mu\text{s}$ -long measurement, with the gate voltage serving as the fast scanning axis. When the average time between two parity jumps exceeds the measurement time but remains shorter than the scan duration, random  $e$ -period shifts appear in the gate response (see overlaid traces in Fig. 2b). When the poisoning rate surpasses the measurement bandwidth, the island switches rapidly between even and odd parity states, producing an  $e$ -periodic signal even within a single trace.

With the detector tuned to the optimal gate bias, we record a series of  $S_{11}$  measurements as a function of the converter bias  $V_c$ . Consecutive measurements are separated by  $20 \mu\text{s}$  to minimize the influence of the readout tone. We determine the optimal phase rotation that encodes the charge parity onto a single quadrature and construct the corresponding histograms as exemplified in the inset of Fig. 2c. At low  $V_c$ , the histograms exhibit a single Gaussian peak, while as  $V_c$  approaches the superconducting gap, they evolve into two well-separated peaks corresponding to the even and odd charge-parity states. The double-peak structure is not accurately described by a simple sum of two Gaussian functions; therefore, we employ a thresholding method to extract the probabilities  $p_0$  and  $p_1$  that the charge parity is even or odd, respectively. Because the two distributions partially overlap, the readout error probabilities  $\epsilon_i$ , corresponding to assigning the opposite outcome  $\bar{i}$  when the true parity is  $i$ , remain significant. We develop a minimal model that includes parity switching during the measurement and estimate  $\epsilon_0 + \epsilon_1 \approx 0.1$ , as detailed in the Supplemental Material.

The evolution of  $p_1$  with  $V_c$  extracted from the histograms is shown in Fig. 2c. The sharp increase beginning near  $400 \mu\text{V}$  marks the onset of elastic quasiparticle tunneling. We attribute the step observed around  $370 \mu\text{V}$  to inelastic tunneling processes involving the absorption of stray photons in a parasitic mode at  $13 \text{ GHz}$ . The probability  $p_1$  increases with higher readout power; however, the use of a JPA enables operation at sufficiently low power to suppress this effect. We also observe that  $p_1$  varies between cooldowns and depends on the charge environment as it shows clear correlation with the evolution of the periodically measured charge offset.

We next repeat the experiment by sending a 18 ns (FWHM) pulse at frequency  $\nu$  onto the detector input, containing on average  $N$  photons per pulse, just before the readout pulse. The detection probability, defined as  $p_1(N) - p_1(0)$ , is plotted in Fig. 3a as a function of  $V_c$ . Distinct steps appear, separated by  $h\nu/e = 41 \mu\text{V}$ , corresponding to PAT processes involving the absorption of  $P = 1, 2,$  and  $3$  photons [32]. We fix  $V_c = 385 \mu\text{V}$ , corresponding to the first step ( $P = 1$ ) below the gap and record  $p_1(N)$  as a function of  $N$ , as shown in Fig. 3b. The calibration of  $N$  is detailed in the Supplemental Material and relies on an independent estimation of the total attenuation between the microwave source and the detector input.

At low photon numbers ( $N \leq 1$ ),  $p_1(N)$  increases linearly with  $N$ , yielding a detection efficiency  $\eta = 8.6\%$ . The efficiency is almost independent of the chosen threshold, which is set at the minimum between the two peaks of the histogram measured at  $N = 0$ . The value of  $\eta$  can be expressed as  $\eta = \text{QE}(1 - 2p_{\text{odd}})(1 - (\epsilon_0 + \epsilon_1))$ , where QE is the quantum efficiency (photon to charge conversion efficiency) and  $p_{\text{odd}}$  is the probability that the island is in an odd-parity state when the photon arrives. Correcting for these effects ( $\epsilon_0 + \epsilon_1 = 0.1$ ,  $p_{\text{odd}} = 0.145$ ) gives an estimated QE  $\approx 13.5\%$ . The detector bandwidth is  $\kappa = 2\pi \times 82 \text{ MHz}$  (see inset in Fig. 3b). A possible explanation for the reduced quantum efficiency relative to the expected value is charge noise in the SCPT, which induces phase noise in the converter mode. Performing the same measurement without the JPA yields a comparable detection efficiency of 9.1%, albeit with a higher dark-count probability (see Supplementary Material).

A key advantage of our detection scheme is its ability to operate in continuous mode. Figure 4a shows time traces of the  $S_{11}$  quadrature encoding the charge parity, sampled with a binning time of 48 ns. The traces exhibit discrete switching between low and high levels, corresponding to the even and odd charge-parity states, respectively. During the measurement, a single pulse containing on average 1.1 photons is applied to the detector input at  $t = 5 \mu\text{s}$ . The averaged trace shown in Fig. 4b displays a sharp transition from even to odd parity coinciding with the pulse arrival, followed by an exponential recovery to the even (ready) state with a characteristic time constant  $\tau = 1.06 \mu\text{s}$ . The relaxation time  $\tau$  varies slightly between cooldowns and depends weakly on  $V_c$  and the readout power, but consistently remains around 1  $\mu\text{s}$  or below.

To reconstruct the time evolution of the charge parity from the measured time traces, we employ a maximum-likelihood reconstruction based on the Viterbi algorithm (see Supplementary Material). The algorithm requires the relaxation and poisoning rates,  $\gamma_{01}$  and  $\gamma_{10}$ , as well as the readout histograms. The rates are determined from the steady-state average parity  $\gamma_{10}/(\gamma_{10} + \gamma_{01})$  and the measured relaxation time  $\tau^{-1} = \gamma_{10} + \gamma_{01}$ . The detection

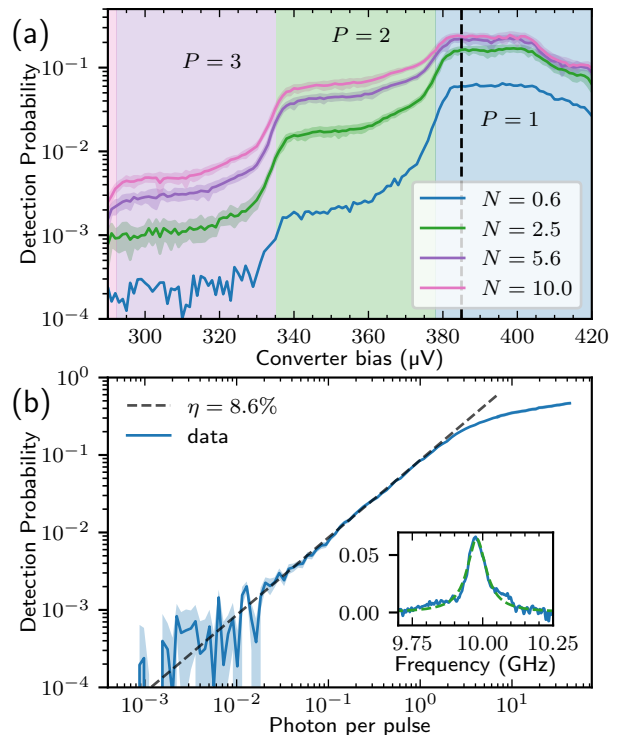


FIG. 3. **Photo-assisted Charge Parity Jump.** (a) Increase in the odd-charge-state probability,  $p_1(N) - p_1(0)$ , after sending a pulse containing  $N$  photons at 10 GHz to the detector input. The colored regions, each of width  $h\nu/e$ , indicate the voltage ranges where  $P$ -photon-assisted tunneling processes are allowed by energy conservation. The shaded area represents the  $1\sigma$  statistical uncertainty. (b) Detection probability  $p_1(N) - p_1(0)$  as a function of  $N$  at  $V_c = 385 \mu\text{V}$  (vertical line in a). The data are obtained with the JPA. Inset: Frequency dependence of the detection probability measured at  $N = 0.8$ ; the Lorentzian fit yields a FWHM linewidth of 82 MHz.

histograms are modeled as two Gaussian distributions. The reconstructed trajectories are overlaid with the measured time traces in Fig. 4a. A rising front (even-to-odd parity transition) identified by the algorithm marks a detection event with a time resolution set by the 48 ns binning time. The single-photon detection efficiency is  $\eta = 10\%$  and the measured dark-count rate of the detector is  $\gamma_{10} = 112 \times 10^3 \text{ s}^{-1}$ . Normalizing by the detection bandwidth and by the efficiency for comparison with other detectors yields  $4\gamma_{10}/(\eta\kappa) = 8.7 \times 10^{-3}$  (see Supplementary Material). From the analysis of numerically generated time traces, we estimate the probability to miss an event to 10% and the probability of false detection to 1.5%.

Figure 4c shows the probability that an event is detected close to the pulse arrival time. No measurable timing jitter is observed beyond the binning resolution. This is consistent with the expected temporal limit set by

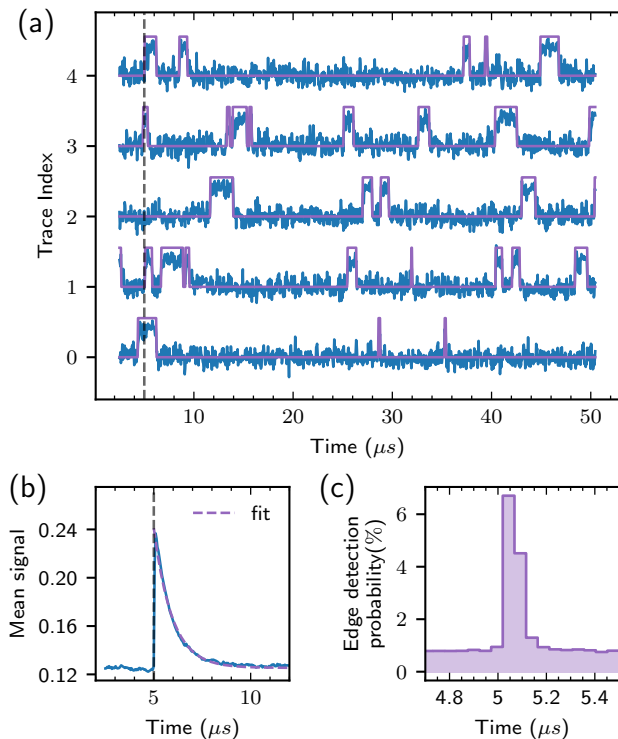


FIG. 4. **Continuous photon detection** (a) Time traces of the readout signal binned with a resolution of 48 ns. The reconstructed charge parity identified by the Viterbi algorithm are shown as purple traces. An incoming pulse with 1.12 photon is applied at  $t = 5 \mu\text{s}$ . (b) Averaged trace obtained from 4096 repetitions of the measurement in (a), showing the pulse arrival and subsequent recovery of the detector. (c) Probability of detecting an even to odd parity jump as a function of time near  $t = 5 \mu\text{s}$ .

the converter cavity linewidth, which determines the rise time of the photo-assisted tunneling (PAT) probability. Based on our estimate of  $\kappa_c$ , we expect only marginal temporal broadening of the pulse width from 18 ns to 20 ns. The readout response can, in principle, follow parity changes almost instantaneously; in practice, its speed is constrained by the detuning induced by a parity jump in the readout resonator, which can be significant.

Finally, we have measured the evolution of the poisoning rate  $\gamma_{10}$  at  $V_c = 385 \mu\text{V}$  as a function of temperature. The data shown in the Supplementary Material are compatible with a quantum efficiency of 56%. This suggests that the quantum efficiency measured at a fixed frequency is likely limited by random fluctuations of the detection band due to charge noise. Under these assumptions, the observed dark count rate corresponds to a residual mode population of  $3 \times 10^{-3}$ . State-of-the-art filtering can suppress populations below  $10^{-5}$  at 10 GHz. Whether such suppression can be achieved in photo-assisted-junction detectors remains an open question.

As such, our detector already stands out for its rapidity compared to state-of-the-art itinerant microwave

photon detectors [4, 9, 10, 18, 21] and by its efficiency relative to other PAT based schemes [18]. Beyond its immediate application to microwave quantum optics and single-photon detection in circuit QED architectures, this detection principle holds promise for quantum-limited readout of mesoscopic systems, fluorescence detection of spin or charge qubits [4, 42], and the search for ultra-weak microwave signals in dark matter axion experiments [43, 44]. In particular, the fast response and low timing jitter make this approach especially suitable for fast qubit readout, time-correlated single-photon detection protocols and quantum optics experiments relying on precise photon arrival statistics. More broadly, this platform also opens new routes for exploring electron-photon interactions in the strong coupling regime.

**Acknowledgements**— We thank P. Bertet, E. Flurin, A. May, C. Di Giorgio for stimulating discussions, B. Reulet for lending us the JPA and R. Weil for technical support during microfabrication. We acknowledge financial support from the ANR (ANR-21-CE47-0010 KIMIDET project), from the France 2030 plan under the ANR-22-PETQ-0003 RobustSuperQ grant, from the Région Ile-de-France in the framework of DIM QuantiP (Quantum Technologies in Paris Region). This work was carried out as part of the NanoLPS micro-nanotechnology platform of the french RENATECH+ network.

\* [julien.basset@universite-paris-saclay.fr](mailto:julien.basset@universite-paris-saclay.fr)

- [1] M. Casariego, E. Zambrini Cruzeiro, S. Gherardini *et al.*, “Propagating quantum microwaves: towards applications in communication and sensing,” *Quantum Sci. Technol.* **8**, 023001 (2023).
- [2] R. H. Hadfield, “Single-photon detectors for optical quantum information applications,” *Nat. Photonics* **3**, 696–705 (2009).
- [3] A. Blais, A. L. Grimsmo, S. M. Girvin, and A. Wallraff, “Circuit quantum electrodynamics,” *Rev. Mod. Phys.* **93**, 025005 (2021).
- [4] E. Albertinale, L. Balembois, E. Billaud *et al.*, “Detecting spins by their fluorescence with a microwave photon counter,” *Nature* **600**, 434–438 (2021).
- [5] J. P. Pekola *et al.*, “Colloquium: Quantum thermodynamics and the nanoscale: The role of quantum coherence,” *Rev. Mod. Phys.* **93**, 041001 (2021).
- [6] K. Inomata, Z. Lin, K. Koshino *et al.*, “Single microwave-photon detector using an artificial Lambda-type three-level system,” *Nat. Commun.* **7**, 12303 (2016).
- [7] A. Opremcak *et al.*, “Measurement of a superconducting qubit with a microwave photon counter,” *Science* **361**, 1239–1242 (2018).
- [8] S. Kono *et al.*, “Quantum non-demolition detection of an itinerant microwave photon,” *Nat. Phys.* **14**, 546–549 (2018).
- [9] J.-C. Besse *et al.*, “Single-shot quantum nondemolition detection of individual itinerant microwave photons,” *Phys. Rev. X* **8**, 021003 (2018).

- [10] R. Lescanne *et al.*, “Irreversible Qubit-Photon Coupling for the Detection of Itinerant Microwave Photons,” *Phys. Rev. X* **10**, 021038 (2020).
- [11] R. Dassonneville, R. Assouly, T. Peronnin, P. Rouchon, and B. Huard, “Number-resolved photcounter for propagating microwave mode,” *Phys. Rev. Appl.* **14**, 044022 (2020).
- [12] A. S. May *et al.*, “Noise Mitigation in Single Microwave Photon Counting by Cascaded Quantum Measurements,” [arXiv:2502.14804](https://arxiv.org/abs/2502.14804) (2025).
- [13] R. Albert, J. Griesmar, F. Blanchet, U. Martel, N. Bourlet, and M. Hofheinz, “Microwave Photon-Number Amplification,” *Phys. Rev. X* **14**, 011011 (2024).
- [14] Y.-F. Chen *et al.*, “Microwave Photon Counter Based on Josephson Junctions,” *Phys. Rev. Lett.* **107**, 217401 (2011).
- [15] G. Oelsner *et al.*, “Detection of Weak Microwave Fields with an Underdamped Josephson Junction,” *Phys. Rev. Appl.* **7**, 014012 (2017).
- [16] A. L. Pankratov *et al.*, “Detection of single-mode thermal microwave photons using an underdamped Josephson junction,” *Nat. Commun.* **16**, 3457 (2025).
- [17] K. Petrovkin *et al.*, “Microwave Photon Detection at Parametric Criticality,” *PRX Quantum* **5**, 020342 (2024).
- [18] S. Haldar *et al.*, “Continuous Microwave Photon Counting by Semiconductor–Superconductor Hybrids,” *Phys. Rev. Lett.* **133**, 217001 (2024).
- [19] F. Oppliger *et al.*, “High-Efficiency Tunable Microwave Photon Detector Based on a Semiconductor Double Quantum Dot Coupled to a Superconducting High-Impedance Cavity,” [arXiv:2506.19828](https://arxiv.org/abs/2506.19828) (2025).
- [20] S. Gasparinetti *et al.*, “Fast electron thermometry for ultrasensitive calorimetric detection,” *Phys. Rev. Appl.* **3**, 014007 (2015).
- [21] R. Kokkonen *et al.*, “Bolometer operating at the threshold for circuit quantum electrodynamics,” *Nature* **586**, 47–51 (2020).
- [22] J. M. Hergenrother *et al.*, “Photon-activated switch behavior in the single-electron transistor with a superconducting island,” *Phys. Rev. B* **51**, 9407 (1995).
- [23] P. M. Echternach *et al.*, “Single-photon detection of 1.5 THz radiation with the quantum capacitance detector,” *Nat. Astron.* **2**, 90–97 (2018).
- [24] R. J. Schoelkopf *et al.*, “The Radio-Frequency Single-Electron Transistor (RF-SET): A Fast and Ultrasensitive Electrometer,” *Science* **280**, 1238–1242 (1998).
- [25] A. Aassime, G. Johansson, G. Wendin, R. J. Schoelkopf, and P. Delsing, “Radio-frequency single-electron transistor as readout device for qubits: Charge sensitivity and backaction,” *Phys. Rev. Lett.* **86**, 3376 (2001).
- [26] M. T. Tuominen, J. M. Hergenrother, T. S. Tighe, and M. Tinkham, “Experimental evidence for parity-based  $2e$  periodicity in a superconducting single-electron tunneling transistor,” *Phys. Rev. Lett.* **69**, 1997 (1992).
- [27] P. Joyez, P. Lafarge, A. Filipe, D. Esteve, and M. H. Devoret, “Observation of parity-induced suppression of Josephson tunneling in the superconducting single-electron transistor,” *Phys. Rev. Lett.* **72**, 2458 (1994).
- [28] A. Amar, D. Song, C. J. Lobb, and F. C. Wellstood, “ $2e$  to  $e$  periodic pair currents in superconducting Coulomb-blockade electrometers,” *Phys. Rev. Lett.* **72**, 3234 (1994).
- [29] A. J. Ferguson, “Microsecond Resolution of Quasiparticle Tunneling in the Single-Cooper-Pair Transistor,” *Phys. Rev. Lett.* **97**, 106603 (2006).
- [30] O. Naaman and J. Aumentado, “Time-domain measurements of quasiparticle tunneling rates in a single-Cooper-pair transistor,” *Phys. Rev. B* **73**, 172504 (2006).
- [31] N. Maleeva *et al.*, “Circuit quantum electrodynamics of granular aluminum resonators,” *Nat. Commun.* **9**, 3889 (2018).
- [32] O. Stanisavljević *et al.*, “Efficient Microwave Photon-to-Electron Conversion in a High-Impedance Quantum Circuit,” *Phys. Rev. Lett.* **133**, 076302 (2024).
- [33] J. Koch and F. von Oppen, “Franck-Condon Blockade and Giant Fano Factors in Transport through Single Molecules,” *Phys. Rev. Lett.* **94**, 206804 (2005).
- [34] C. Bergenfeldt and P. Samuelsson, “Microwave quantum optics and electron transport through a metallic dot strongly coupled to a transmission line cavity,” *Phys. Rev. B* **85**, 045446 (2012).
- [35] J. P. Pekola *et al.*, “Single-electron current sources: Toward a refined definition of the ampere,” *Rev. Mod. Phys.* **85**, 1421 (2013).
- [36] M. H. Devoret, D. Esteve, H. Grabert, G.-L. Ingold, H. Pothier, and C. Urbina, “Effect of the electromagnetic environment on the Coulomb blockade in ultrasmall tunnel junctions,” *Phys. Rev. Lett.* **64**, 1824 (1990).
- [37] G.-L. Ingold and Y. V. Nazarov, “Charge tunneling rates in ultrasmall junctions,” in *Single Charge Tunneling*, ed. by H. Grabert and M. H. Devoret (NATO ASI Series B, Vol. 294, Plenum, New York, 1992).
- [38] J. Aumentado, M. W. Keller, J. M. Martinis, and M. H. Devoret, “Nonequilibrium quasiparticles and  $2e$  periodicity in single-Cooper-pair transistors,” *Phys. Rev. Lett.* **92**, 066802 (2004).
- [39] H. Brenning, S. Kafanov, T. Duty, S. Kubatkin, and P. Delsing, “An ultrasensitive radio-frequency single-electron transistor working up to 4.2 K,” *J. Appl. Phys.* **100**, 114321 (2006).
- [40] K. Serniak *et al.*, “Direct Dispersive Monitoring of Charge Parity in Offset-Charge-Sensitive Transmons,” *Phys. Rev. Appl.* **12**, 014052 (2019).
- [41] K. R. Amin *et al.*, “Direct detection of quasiparticle tunneling with a charge-sensitive superconducting sensor coupled to a waveguide,” [arXiv:2404.01277](https://arxiv.org/abs/2404.01277) (2024).
- [42] Z. Wang, L. Balembois, M. Rančić *et al.*, “Single-electron spin resonance detection by microwave photon counting,” *Nature* **619**, 276–281 (2023).
- [43] P. Sikivie, “Invisible axion search methods,” *Rev. Mod. Phys.* **93**, 015004 (2021).
- [44] A. L. Pankratov, L. S. Revin, A. V. Gordeeva *et al.*, “Towards a microwave single-photon counter for searching axions,” *npj Quantum Inf.* **8**, 61 (2022).

### Sample Fabrication

The device shown in Fig. 1 of the main text is fabricated using a combination of optical and electron-beam lithography. In the first step, electron-beam lithography defines 700 nm-wide, 20 nm-thick granular aluminium (GrAl) nanowires, deposited by e-gun evaporation with a small partial pressure of oxygen and patterned by lift-off. A second electron-beam lithography step is then used to define the three tunnel junctions and the superconduct-

ing island. Aluminium is first evaporated at normal incidence to a thickness of 15 nm, followed by a controlled oxidation for 15 minutes at 10 mbar. A second evaporation at a positive angle deposits 30 nm of Al to form the more transparent junctions (readout and drain), followed by a double oxidation step separated by a 0.2 nm Al flash, and finally a third evaporation of 65 nm Al at a negative angle. All evaporations are performed without breaking vacuum and followed by lift-off. In a final step, optical lithography defines the aluminium transmission lines and contact pads connecting the GrAl resonators and the junction region, deposited by a 120 nm Al evaporation.

### Estimation of the photo-assisted tunneling (PAT) rate

The PAT rate through the converter junction is determined by both the junction transparency and its electromagnetic environment. We first compute the  $I(V)$  characteristic of the converter junction (JC) using the standard density of states for a SIS junction and the measured large-bias resistance of  $6.4 \text{ M}\Omega$ . From this, we obtain a tunneling current of  $I_T = 53 \text{ pA}$  for a bias a few  $\mu\text{V}$  above the gap.

The electromagnetic environment of the junction is set on one side by the modes of the grAl wire resonator and on the other side by the modes of the Cooper pair box. For simplicity, we neglect coupling between the two sets of modes. The converter-mode spectrum is obtained by modeling the grAl wire with a capacitance per unit length of  $41.7 \text{ pF m}^{-1}$  and an inductance per unit length of  $714 \text{ }\mu\text{H m}^{-1}$ . A  $3.75 \text{ pF}$  capacitance to ground is added to account for the SET at the end of the resonator. This yields the following resonance frequencies and characteristic impedances:

Frequency (GHz)	Impedance (k $\Omega$ )	$\lambda$ factor
10.02	3.27	0.63
42.48	0.13	0.12

Higher-order modes contribute negligibly to the impedance. The Franck–Condon coefficient for the inelastic tunneling process in which one photon is absorbed from the first mode while the second mode remains in vacuum is

$$\alpha = \lambda_0^2 e^{-\lambda_0^2} e^{-\lambda_1^2} \approx 0.26, \quad (\text{S.1})$$

with  $\lambda_0 = 0.63$  and  $\lambda_1 = 0.12$ . On the opposite side of the junction, quantum phase fluctuations of the island further reduce the tunneling rate. The island is described by the Hamiltonian

$$H = 4E_C(n - n_g)^2 - E_J \cos \varphi, \quad (\text{S.2})$$

where  $n$  and  $\varphi$  are the conjugate variables for the island Cooper-pair number and phase, and  $n_g$  is the gate-induced offset charge. The reduction of the quasiparticle tunneling rate is governed by the phase-fluctuation

factor  $|\langle e^{i\varphi/2} \rangle|^2$ . The factor  $1/2$  accounts for the quasiparticle charge being half that of a Cooper pair. Assuming a Gaussian ground state, we use the relation  $|\langle e^{i\varphi/2} \rangle| = |\langle e^{i\varphi} \rangle|^{1/4}$ . We evaluate the ground state of  $H$  in the charge basis  $|n\rangle$ , in which  $e^{i\varphi}$  acts as the shift operator  $|n+1\rangle\langle n|$ . Close to  $n_g = 0.5$ , we obtain  $|\langle e^{i\varphi} \rangle| = 0.56$  for  $E_J = E_C = 2\pi \times 4.6 \text{ GHz}$ . The PAT rate is therefore

$$\kappa_j = \alpha |\langle e^{i\varphi} \rangle|^{1/2} \frac{I_T}{e} = 2\pi \times 10.3 \text{ MHz}. \quad (\text{S.3})$$

### Measurement setup

A schematic of the experimental setup is shown in Fig. S1. The device is mounted in a copper sample box equipped with a microwave printed circuit board, indium sealed, and thermally anchored to the mixing-chamber plate of a dilution refrigerator operating at a base temperature of 20 mK. To allow simultaneous dc biasing and microwave measurements, the device is connected to the measurement circuit through a diplexer (or bias tee). Microwave characterization of readout and converter lines are performed using a vector network analyzer or a quantum machine. The excitation signal is routed to the sample through an attenuated input line, while the reflected signal is directed to the output line through a series of circulators and amplifiers. The reflected signal is first either amplified by a JPA that works in reflection (the components enclosed by the dashed rectangle in Fig. S1 indicate the optional JPA setup), or directly connected to a low-noise HEMT amplifier at 4 K, followed by two room-temperature amplifiers. The junctions and the gate are voltage-biased via voltage dividers and filtering capacitors connected to the low-frequency ports of the diplexer/bias tee at base temperature. The biasing circuits involve  $50 \text{ k}\Omega$  and  $200 \text{ k}\Omega$  series resistor for reliable circuit biasing.

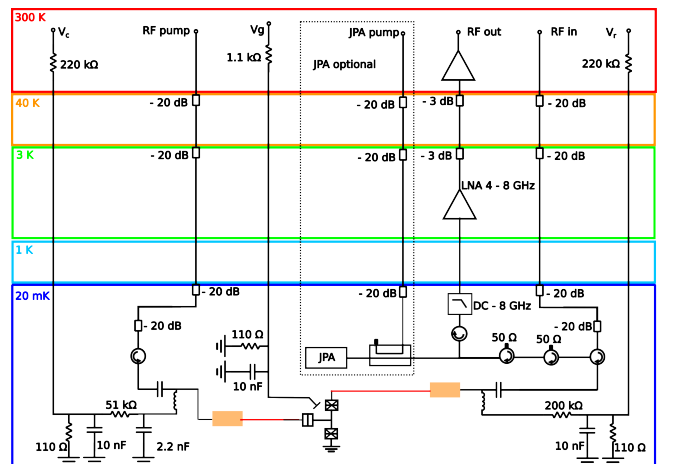


FIG. S1. Schematic of the measurement setup cabled in the dilution refrigerator.

### Estimation of the readout error

As stated in the main text and shown in figure S2, the probability distribution of the measured quadrature is not well fitted by the sum of two gaussian functions, one for each parity state. We attribute this to the fact that the parity changes during the measurement time  $T$ . In order to model this effect, we suppose that the

$$\begin{aligned}
 P_1(x) &= \int_0^T \frac{\gamma_{01} e^{-\gamma_{01}t}}{\sqrt{2\pi\sigma_1^2}} e^{-\frac{[x-(t/T)c_1-(1-t/T)c_0]^2}{2\sigma_1^2}} dt + \frac{e^{-\gamma_{01}T}}{\sqrt{2\pi\sigma_1^2}} e^{-\frac{(x-c_1)^2}{2\sigma_1^2}} \\
 &= \frac{\gamma_{01}T}{2(c_0 - c_1)} \left\{ \left[ \operatorname{erf}\left(\frac{c_0^2 - c_0(c_1 + x) + c_1x - \gamma_{01}\sigma_1^2T}{\sqrt{2}\sigma_1(c_0 - c_1)}\right) - \operatorname{erf}\left(\frac{\gamma_{01}\sigma_1T}{\sqrt{2}(c_1 - c_0)} + \frac{c_1 - x}{\sqrt{2}\sigma_1}\right) \right] \right. \\
 &\quad \left. \times \exp\left[\frac{\gamma_{01}T(\gamma_{01}\sigma_1^2T - 2(c_0 - c_1)(c_0 - x))}{2(c_0 - c_1)^2}\right] \right\} + \frac{e^{-\gamma_{01}T}}{\sqrt{2\pi\sigma_1^2}} e^{-\frac{(x-c_1)^2}{2\sigma_1^2}}. \tag{S.4}
 \end{aligned}$$

If the initial parity is even, we obtain the distribution  $P_0(x)$  in the same way with  $\gamma_{01} \rightarrow \gamma_{10}$ ,  $\sigma_0 \rightarrow \sigma_1$  and  $c_0 \leftrightarrow c_1$ . The measured histogram is fitted by a weighted sum  $wP_0(x) + (1-w)P_1(x)$ , leaving  $w$ ,  $c_0$ ,  $c_1$ ,  $\sigma_0$ ,  $\sigma_1$  as free parameters and fixing  $\gamma_{01} = \gamma_{10} = 0.94(1.7) \mu\text{s}^{-1}$  with (without) JPA. In principle,  $\sigma_0$  and  $\sigma_1$  should be identical, but the data are better fit when they are allowed to differ. Fixing the threshold to  $x_{\text{threshold}}$ , the readout errors are given by

$$\epsilon_0 = \int_{x_{\text{threshold}}}^{\infty} P_0(x) dx \quad \epsilon_1 = \int_{-\infty}^{x_{\text{threshold}}} P_1(x) dx.$$

Figure S2 shows the histogram of the readout signal measured with JPA at  $V_c = 385 \mu\text{V}$  in the absence of incoming photons ( $N = 0$ ). Setting the threshold at the local minimum between the two peaks, we obtain  $w = 0.96$ ,  $\epsilon_0 = 3.0\%$ ,  $\epsilon_1 = 6.3\%$  with JPA and  $w = 0.86$ ,  $\epsilon_0 = 6.4\%$ ,  $\epsilon_1 = 13.2\%$  without JPA.

### Power calibration

The calibration of the number of photons per pulse first relies on a quantitative measurement of the output pulse from the microwave source characterized at room temperature using a calibrated spectrum analyzer in zero span mode. Each recorded pulse trace is fitted to a Gaussian profile, from which we extract the pulse energy  $E_{\text{pulse}}$  as the integral of the fitted function. We then determine the total attenuation  $A_{\text{tot}}$  of the microwave lines and components through a series of vector network analyzer (VNA) measurements. First, the attenuation of the room-temperature section of the setup, including filters,

mean signal is  $c_0$  ( $c_1$ ) if the parity is even (odd), that the parity switches from  $j$  to  $i$  at a rate  $\gamma_{ij}$  and that the measurement noise is set by the amplifier noise to a rms value  $\sigma$ . We suppose that only one parity jump can happen during the measurement time. If the initial parity is odd, the probability to obtain the outcome  $x$  is a sliding gaussian distribution given by

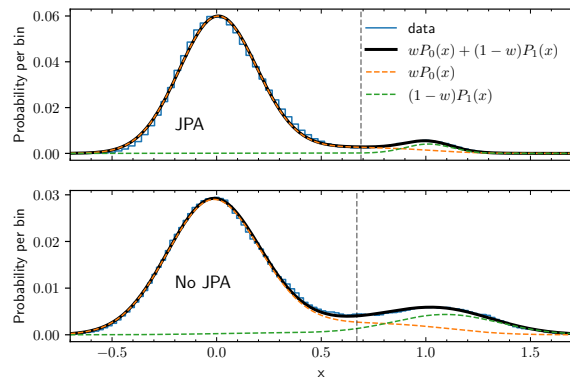


FIG. S2. Histograms at  $V_c = 385 \mu\text{V}$  and  $N = 0$  with (upper panel) and without JPA (lower panel) and fit using a weighted sum of two sliding gaussian distributions (eq. S.4). The vertical dashed line indicates the threshold set at the local minimum between the two peaks.

cables, and dc blocks, is measured, yielding the value  $A_0$ . The attenuation of the cryostat cables,  $A_1$ , is obtained by measuring in series the transmission through the pump line of interest and a nominally identical return line (same length, attenuators, and cable type);  $A_1$  is then taken as half of the total measured attenuation. Finally, the attenuation at the mixing-chamber stage,  $A_2$ , is evaluated from direct VNA measurement of the full cryogenic assembly, including circulators, diplexer, attenuators, and cables leading to the chip at room temperature. The overall attenuation of the complete line is taken to be  $A_{\text{tot}} = A_0 + A_1 + A_2 = 90.6 \pm 0.5 \text{ dB}$  at  $\nu = 9.97 \text{ GHz}$ . The average number of photons per pulse at the device input is then obtained from  $N = \frac{E_{\text{pulse}} \times 10^{-A_{\text{tot}}/10}}{h\nu}$ .

### Viterbi algorithm

The island's charge parity undergoes random transitions between even and odd states at fixed rates  $\gamma_{01}$  and  $\gamma_{10}$ , forming a two-state Markov process. Labeling the parity at times  $t_i$  as  $q_i$ , the likelihood of obtaining a sequence of observations  $x_i$  is

$$P(X|Q) = \prod_{i=1}^T P(x_i|q_i) \quad (\text{S.5})$$

where  $T$  is the number of measurements and  $X$  and  $Q$  denote the two sequences  $\{x_i\}$  and  $\{q_i\}$ , respectively. The conditional probabilities  $P(x|0) \equiv P_0(x)$  and  $P(x|1) \equiv P_1(x)$  are supposed to be known. Here we approximate them as Gaussian distributions whose parameters are extracted by fitting the histogram of  $X$ . The Viterbi algorithm determines the most likely parity sequence  $Q$  that generated the observations  $X$  [S1]. Denoting the binning time by  $dt = t_{i+1} - t_i$ , the pseudocode of the algorithm is

```

w00 ← exp(-γ10 * dt)
w11 ← exp(-γ01 * dt)
w10 ← 1 - w00
w01 ← 1 - w11
p0[1] ← γ01 / (γ01 + γ10) * P1(x1)
p1[1] ← γ10 / (γ01 + γ10) * P0(x1)
normalize(p0[1], p1[1])
for i = 2, 3, ..., T do
  p00 ← w00 * p0[i - 1]
  p01 ← w01 * p1[i - 1]
  if p01 > p00 then
    p0[i] ← p01 * P0(xi)
    b[i, 0] ← 1
  else
    p0[i] ← p00 * P0(xi)
    b[i, 0] ← 0
  p10 ← w10 * p0[i - 1]
  p11 ← w11 * p1[i - 1]
  if p11 > p10 then
    p1[i] ← p11 * P1(xi)
    b[i, 1] ← 1
  else
    p1[i] ← p10 * P1(xi)
    b[i, 1] ← 0
  normalize(p0[i], p1[i])
if p1[T] > p0[T] then
  q[T] ← 1
else
  q[T] ← 0
for i = T - 1, T - 2, ..., 1 do
  q[i] ← b[i + 1, q[i + 1]]
return q

```

The purpose of the normalize function is to rescale its arguments so that their sum is equal to unity.

### Temperature dependent poisoning

We assume that the intrinsic losses of the converter resonator are negligible compared with the coupling loss  $\kappa_c$  and the PAT rate  $\kappa_j$ . Under this assumption, the detection efficiency is  $\eta = 4\kappa_j\kappa_c / (\kappa_j + \kappa_c)^2$ . In the absence of an incoming signal, the steady-state population of the resonator is purely thermal, with an average photon number  $n_{\text{th}} = \kappa_c(n_{\text{BE}}(T) + n_0) / (\kappa_c + \kappa_j)$ , where  $n_{\text{BE}}(T) = (e^{h\nu/kT} - 1)^{-1}$  is the Bose-Einstein distribution at frequency  $\nu = 10$  GHz,  $n_0$  is a residual out of equilibrium population and the junction is modeled as a zero-temperature bath [S2]. The resulting poisoning rate is given by

$$\gamma_{10} = \kappa_j n_{\text{th}} = \frac{\eta \kappa}{4} (n_{\text{BE}}(T) + n_0). \quad (\text{S.6})$$

where  $\kappa = \kappa_c + \kappa_j = 2\pi \times 81.6$  MHz is the measured linewidth. Figure S3 shows the measured evolution of  $\gamma_{10}$  as a function of temperature. Fitting the data with Eq. (S.6) yields  $\eta = 56\%$  and  $n_0 = 3 \times 10^{-3}$ .

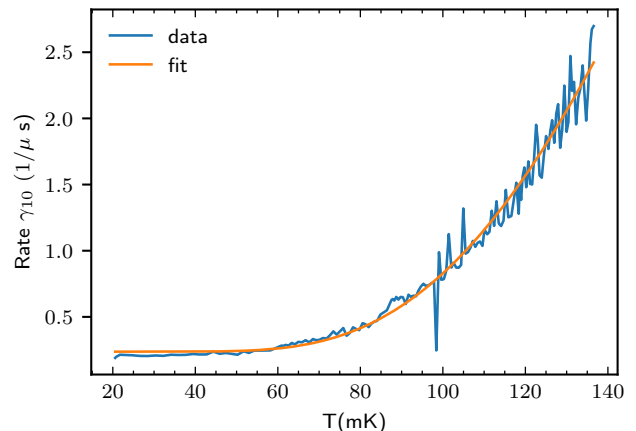


FIG. S3. Temperature dependence of the poisoning rate  $\gamma_{10}$ . The solid orange line is a fit to the data using Eq. (S.6).

### SUPPLEMENTARY CITATIONS

- [S1] O. Stanisavljević *et al.*, “Efficient Microwave Photon-to-Electron Conversion in a High-Impedance Quantum Circuit,” *Phys. Rev. Lett.* **133**, 076302 (2024).
- [S2] A. Viterbi, “Error bounds for convolutional codes and an asymptotically optimum decoding algorithm,” *IEEE Trans. Inf. Theory* **13**, 260 (1967).